RESEARCH Open Access

# The Evolution of Concrete Microstructure and Chloride-Ion Diffusion Coefficient Under Cyclic Axial Compression



Qingzhang Zhang<sup>1,2</sup>, Mengzhe Zhao<sup>2</sup>, Li Song<sup>3\*</sup>, Yuhang Yang<sup>2</sup> and Jiaming He<sup>2</sup>

### **Abstract**

The changes of the microscopic pore structure for concrete under cyclic axial compression accelerate chloride-ion penetration, reducing the durability of concrete structures. To address this, a chloride-ion migration experiment for concrete was conducted under cyclic axial compression, and the pore structure and pore group content of concrete were quantitatively characterized through equilibrium moisture content testing. In addition, a multiscale theoretical model for the chloride-ion diffusion coefficient in concrete was established based on the multiphase sphere model. The results show that cyclic loading forms an open hysteresis loop in the concrete's stress-strain curve, which evolves in the direction of increasing strain. Under loading, the microscopic pore structure of concrete coarsens, with an increase in the proportion of large capillary pores and gel pores, and a decrease in the proportion of small capillary pores. The model demonstrates good applicability when the chloride-ion diffusion coefficient is less than  $22 \times 10^{-12}$  m<sup>2</sup>/s. The model analysis indicates that the influence of cyclic axial compression loading on chlorideion diffusion coefficient is more pronounced when the initial porosity ranges from 0.1 to 0.3. In addition, the more complex the microstructure of the concrete, the less its chloride-ion diffusion coefficient is affected by load-induced damage. At the same  $D_l/D_m$  ratio,  $D_c/D_m$  gradually decreases with increase the volume fraction of coarse aggregates, but when  $D_l/D_m$  reaches 15, the variation of  $D_c/D_m$  becomes negligible, approximately equal to 0.86. This indicates that when the ITZ exhibits a higher porosity content, the increased availability of chloride-ion transport pathways counteracts the blocking effect of coarse aggregates on chloride ions.

**Keywords** Cyclic axial compression loading, Damaged concrete, Pore structure, Chloride ions, Diffusion coefficient

Journal information: ISSN 1976-0485 / eISSN 2234-1315.

\*Correspondence:

Li Song

songlisong2008@163.com

<sup>1</sup> Henan Key Laboratory of Grain and Oil Storage Facility & Safety, Henan University of Technology, Zhengzhou 450001, Henan, China

<sup>2</sup> College of Civil Engineering, Henan University of Technology, Zhenazhou 450001, Henan, China

<sup>3</sup> National Engineering Research Center of High-Speed Railway Construction Technology, Changsha 410075, Hunan, China

### 1 Introduction

In coastal environments, chloride-ion ingress is the primary cause of steel reinforcement corrosion and durability degradation in concrete. Concrete structures in marine environments are subjected to cyclic loading, which leads to the accumulation of internal damage and changes in the microscopic pore structure of the concrete. This causes the propagation and interconnection of primary microcracks, and generates new secondary cracks at areas with weak matrix bonding, providing more pathways for chloride-ion transport. This accelerates chloride-ion penetration, thus reducing the concrete structure's resistance to chloride-ion corrosion (Liu et al., 2022).



© The Author(s) 2025. **Open Access** This article is licensed under a Creative Commons Attribution-NonCommercial-NoDerivatives 4.0 International License, which permits any non-commercial use, sharing, distribution and reproduction in any medium or format, as long as you give appropriate credit to the original author(s) and the source, provide a link to the Creative Commons licence, and indicate if you modified the licensed material. You do not have permission under this licence to share adapted material derived from this article or parts of it. The images or other third party material in this article are included in the article's Creative Commons licence, unless indicated otherwise in a credit line to the material. If material is not included in the article's Creative Commons licence and your intended use is not permitted by statutory regulation or exceeds the permitted use, you will need to obtain permission directly from the copyright holder. To view a copy of this licence, visit <a href="https://creativecommons.org/licenses/by-nc-nd/4.0/">https://creativecommons.org/licenses/by-nc-nd/4.0/</a>.

Saito et al. (2020) conducted experiments on chlorideion migration in concrete under axial compression and found that compressive stress below a stress level threshold (50%) reduced the chloride-ion transport rate. While the stress level exceeded this threshold, the transport rate significantly increased. This finding is consistent with the research by Lee et al. (2014), who discovered that with an increase in load-induced damage, the residual axial strain of concrete specimens increased, and the chloride-ion diffusion coefficient increased by 1.5 times. Furthermore, the study by Fu et al. (2016) showed that when the stress level was between 25 and 45% of the specimen's ultimate tensile load, tensile fatigue damage could accelerate chloride-ion penetration in concrete by 1.5 to 3.0 times. From the aforementioned studies, it can be observed that although the variation in chloride-ion transport performance is significant under different stress levels, it is difficult to establish a direct relationship between the applied load and chloride-ion transport performance due to the wide range of stress levels and the lack of a clear correlation between them.

Through mercury intrusion porosimetry (MIP) and scanning electron microscopy (SEM) tests that the total volume of capillary pores, Li et al. (2020) found critical pore diameter, and fractal dimension are positively correlated with the chloride-ion diffusion coefficient, indicating a close relationship between the chloride-ion diffusion coefficient and the microscopic structure of concrete. In addition, Yang et al. (2006) further pointed out that there is a linear relationship between the interconnected pore diameter in concrete and the chlorideion diffusion coefficient, which supports the influence of the microstructure on chloride-ion diffusion behavior. Furthermore, Zhang et al. (2018) investigated the chloride-ion transport performance of concrete under loading from perspective of pore structure by applying volumetric change rate and dynamic elastic modulus, This provides a new perspective for studying the chloride-ion transport mechanism under loading. In relation to this, Du et al. (2015) discovered that the chloride-ion diffusion coefficient of cement mortar increases significantly with initial porosity, but decreases with the increase in compressive volumetric strain. This shows the complex relationship between pore structure and diffusion coefficient. Moreover, Guan et al. (2018) characterized the chloride-ion diffusion coefficient of concrete based on the crack area and established a chloride-ion transport model under loading from a microscopic perspective. To more accurately predict chloride ion diffusion coefficient of cement mortar, He et al. (2020) proposed a two-stage model based on the porosity and effective medium model (GEM) to predict the effective chloride diffusion coefficient of cement mortar, and the model predictions were in good agreement with the experimental values. Tong et al. (2024) proposes a novel multiscale framework for modeling chloride penetration in concrete, incorporating pore structure-dependent parameters by linking chloride diffusivities with pore size distributions (PSDs). Jin et al. (2023). concluded that as the number of wet–dry cycles increased, the cumulative pore size and maximum probability pore size of concrete gradually increased, leading to more significant pore structure deterioration and reduced compactness, which accelerated chloride migration in the matrix.

In summary, the current research has revealed the significant influence of loading and microstructure on the chloride-ion transport performance of concrete. However, due to the complex interactions between stress levels, pore structure characteristics, and diffusion coefficients, a comprehensive chloride-ion diffusion model that considers the effects of multiple factors has yet to be fully developed. Therefore, this paper first investigated the deformation evolution of concrete under cyclic loading by monitoring the stress-strain curves of concrete specimens during loading and unloading processes. Then, based on the equilibrium moisture content tests, the pore structure parameters of concrete specimens under different loading conditions were analyzed using the density function method and pore size distribution function. Finally, a multiscale theoretical model was established to account for the effects of cyclic loading and microstructure on the chloride-ion diffusion coefficient of concrete. The effects of cyclic loading and microstructure changes on chloride diffusion coefficient of concrete were investigated.

### 2 Theoretical Model of Chloride-Ion Diffusion Coefficient in Concrete Under Cyclic Loading

### 2.1 Microscale Theoretical Model of Porosity in Damaged Cement Mortar

Under external loading, the porosity within cement mortar is undergone significant changes, and these pores serve as the primary channels for chloride-ion transport, affecting chloride-ion transport performance directly (Liu et al., 2019). Therefore, the impact of external loading on the chloride-ion diffusion coefficient in cement mortar can be regarded as the effect of porosity changes on its diffusion performance. According to reference (Du et al., 2015), at the microscale, concrete can be assumed to be a two-phase composite material composed of a cement mortar matrix, different scales of pores, and microcracks. Assuming the cement mortar matrix and pores are spherical, the damaged porosity  $\phi_{\rm m}$  of the cement mortar under loading can be obtained, as shown in Fig. 1.

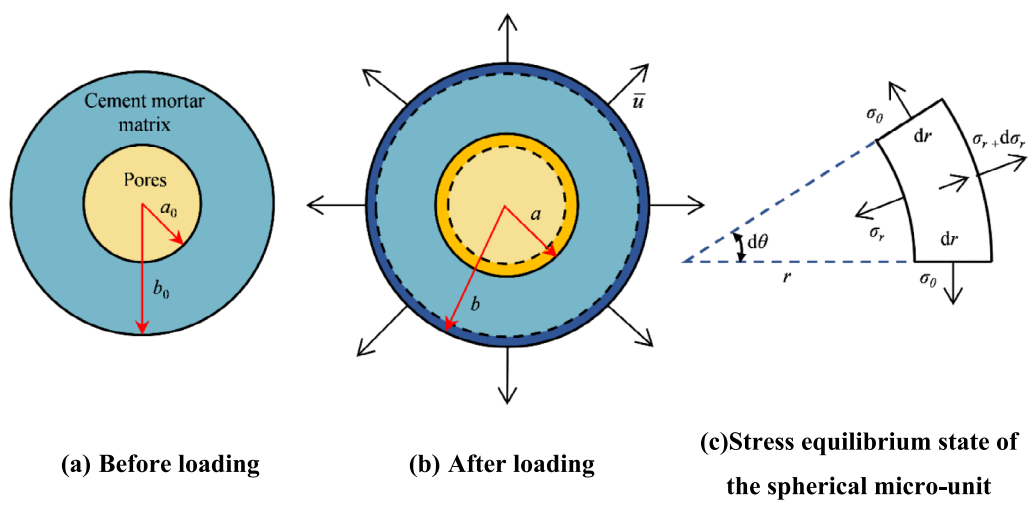


Fig. 1 Schematic diagram of the two-phase spherical model of cement mortar and pores under load

When the spherical model of cement mortar is subjected to external loading, resulting in a uniform forced displacement  $\ddot{\mathbf{u}}$ , its deformation behavior is illustrated in Fig. 1b. Assuming the cement mortar matrix is isotropic, the initial porosity  $\phi_0$  can be expressed as:

$$\varphi_0 = \left(\frac{a_0}{b_0}\right)^3 \tag{1}$$

In Eq. (1),  $a_0$  represents the initial inner radius (mm), and  $b_0$  represents the initial outer radius (mm).

The damaged porosity of cement mortar after the application of load is expressed as:

$$\varphi_{\rm m} = \left(\frac{a}{h}\right)^3 \tag{2}$$

In Eq. (2), *a* represents the inner radius after the application of load (mm), and b represents the outer radius after the application of load (mm).

The cement mortar model is subjected to radial forced displacement  $\tilde{u}$  can be represented by the basic differential equation of a hollow elastic sphere due to the symmetry of its geometry and the externally applied displacement:

$$\frac{E(1-\nu)}{(1+\nu)(1-2\nu)} \left( \frac{d^2 u_{\rm r}}{dr^2} + \frac{2}{r} \frac{du_{\rm r}}{dr} - \frac{2}{r^2} u_{\rm r} \right) + f_{\rm r} = 0$$
(3)

In Eq. (3),  $u_r$  represents the radial displacement component of the sphere (mm),  $f_r$  is the radial body force (N), r is the distance from the boundary to the center of the sphere (mm),  $\nu$  is the Poisson's ratio of the solid phase matrix material, and E is the elastic modulus of the solid phase matrix material (GPa).

The stress equilibrium state of the hollow spherical microelement is illustrated in Fig. 1c. The stress components in Eq. (3) can be expressed as:

$$\begin{cases}
\sigma_{\rm r} = \frac{E}{(1+\nu)(1-2\nu)} \left[ (1-\nu)\frac{du_{\rm r}}{dr} + 2\nu\frac{u_{\rm r}}{r} \right] \\
\sigma_{\theta} = \frac{E}{(1+\nu)(1-2\nu)} \left[ \nu\frac{du_{\rm r}}{dr} + \frac{u_{\rm r}}{r} \right]
\end{cases} (4)$$

In Eq. (4),  $\sigma_r$  represents the radial stress component, and  $\sigma_{\theta}$  represents the axial stress component.

In the absence of radial body forces, the partial differential equation for radial displacement in a spherical polar coordinate system can be expressed as (Zhang et al., 2021):

$$\frac{d^2u_{\rm r}}{dr^2} + \frac{2}{r}\frac{du_{\rm r}}{dr} - \frac{2}{r^2}u_{\rm r} = 0 \tag{5}$$

The radial displacement field  $u_{\rm rm}$  and the radial stress field  $\sigma_{\rm rm}$  of the cement mortar matrix can be obtained from Eq. (4) and (5), respectively:

$$\begin{cases} u_{\rm rm} = A_{\rm m} \times r + \frac{B_{\rm m}}{r^2} \\ \sigma_{\rm rm} = 3K_{\rm m}A_{\rm m} - \frac{4\mu_{\rm m}B_{\rm m}}{r^3} \end{cases}$$
 (6)

In Eq. (6),  $K_{\rm m}$  represents the bulk modulus of the cement mortar phase (GPa),  $\mu_{\rm m}$  denotes the shear modulus of the cement mortar phase (GPa), and  $A_{\rm m}$  and  $B_{\rm m}$  are the undetermined parameters.

In addition, the radial displacement field  $u_{\rm rp}$  and the radial stress field  $\sigma_{\rm rp}$  of the spherical pores can be expressed as:

$$\begin{cases} u_{\rm rp} = A_{\rm p} \times r \\ \sigma_{\rm rp} = 3K_{\rm p}A_{\rm p} \end{cases}$$
 (7)

In Eq. (7),  $K_p$  represents the bulk modulus of the pore medium (GPa), and  $A_p$  is an undetermined parameter.

Since the stress distribution within the two-phase sphere is symmetrical, the boundary conditions of the computational model can be expressed as:

$$\begin{cases} u_{\rm rm}|_{r=b_0} = \overline{u} \\ u_{\rm rm}|_{r=a_0} = u_{\rm rp}|_{r=a_0} \\ \sigma_{\rm rm}|_{r=a_0} = \sigma_{\rm rp}|_{r=a_0} \end{cases}$$
(8)

Under the enforced displacement  $\bar{u}$ , the volumetric strain  $\varepsilon_v$  of the two-phase sphere can be calculated as:

$$\varepsilon_{\rm v} = 1 - (1 - \frac{\overline{u}}{b_0})^3 \tag{9}$$

By substituting Eq. (8) into Eqs. (6) and (7) yields:

$$\begin{cases} A_{\rm m} = \frac{p \times \Theta}{p + 3\lambda \times \varphi_0} \\ B_{\rm m} = \frac{3\lambda a_0^3 \times \Theta}{p + 3\lambda \times \varphi_0} \\ A_{\rm p} = \frac{(3\lambda + p) \times \Theta}{p + 3\lambda \times \varphi_0} \end{cases}$$
(10)

In the equation,  $\Theta=1-\sqrt[3]{1-\varepsilon_{\rm V}}$ ,  $\lambda=K_{\rm m}-K_{\rm p}$ ,  $p=3K_{\rm p}+4\mu_{\rm m}$ .

By substituting Eq. (10) into Eq. (6), the radial displacement at  $r = a_0$  can be expressed as:

$$u_{\rm rm}|_{r=a_0} = \frac{(3\lambda + p) \times \Theta}{p + 3\lambda \times \varphi_0} \times a_0 \tag{11}$$

Therefore, under the enforced displacement  $\bar{u}$ , the damaged porosity  $\phi_{\rm m}$  of the cement mortar can be calculated as:

$$\varphi_{\rm m} = \left(\frac{a}{b}\right)^3 = \frac{a_0^3}{\left(b_0 - \overline{u}\right)^3} \times \left[1 - \frac{(3\lambda + p) \times \Theta}{p + 3\lambda \times \varphi_0}\right]^3$$
(12)

By simultaneously considering Eqs. (1), (9), (12), (13) can be simplified to:

$$\varphi_{\rm m} = \frac{\varphi_0}{1 - \varepsilon_{\rm v}} \times \left[ 1 - \frac{(3\lambda + p) \times \Theta}{p + 3\lambda \times \varphi_0} \right]^3 \tag{13}$$

From Eq. (13), it can be seen that the damaged porosity  $\phi_{\rm m}$  of the cement mortar, the initial porosity  $\phi_0$ , and the volumetric strain  $\varepsilon_{\rm v}$  are closely related. The volumetric strain is calculated using the residual strain of the loaded concrete specimens, and a damage variable  $D_{\rm s}$  is

introduced to account for the cyclic plastic damage in the model. The effective bulk modulus  $K^*$  and shear modulus  $\mu^*$  of the cement mortar element are expressed as follows:

$$\begin{cases} K^* = \frac{E_{\rm m}(1 - D_{\rm s})}{3(1 - 2\nu)} \\ \mu^* = \frac{E_{\rm m}(1 - D_{\rm s})}{2(1 + \nu)} \end{cases}$$
(14)

In Eq. (14),  $E_{\rm m}$  represents the initial elastic modulus of the cement mortar element (GPa), and  $\nu$  denotes the Poisson's ratio of the cement mortar element.

If the effects of the thickness of the concrete interfacial transition zone and the interaction between aggregates are not considered, the enforced displacement  $\bar{u}$  under axial stress can be expressed as follows:

$$\overline{u} = L\varepsilon \tag{15}$$

In the equation, L represents the axial length of the specimen (mm), and  $\varepsilon$  denotes the strain under uniaxial loading, corresponding to the residual strain in this study.

Let the initial loading elastic modulus of concrete be  $E_0$  and the unloading elastic modulus at the current cycle be E. The damage variable  $D_{\rm s}$  under cyclic loading can be expressed as (Jin, 2012):

$$D_{\rm s} = 1 - \frac{E}{E_0} \tag{16}$$

In the equation, the dynamic elastic modulus *E* can be obtained from the real-time monitored stress–strain curve, as expressed in the following equation (Rao & Ramana, 1992):

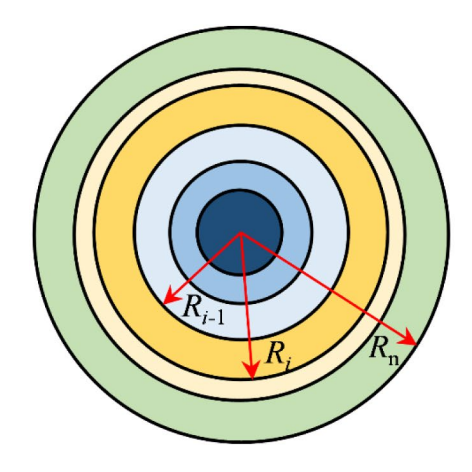
$$E = \frac{(\sigma_{\text{max}} - \sigma_{\text{min}})}{(\varepsilon_{\text{max}} - \varepsilon_{\text{min}})} \tag{17}$$

In Eq. (17),  $\sigma_{\rm max}$  and  $\sigma_{\rm min}$  represent the maximum and minimum stresses of the unloading curve during a single cycle, while  $\varepsilon_{\rm max}$  and  $\varepsilon_{\rm min}$  denote the upper and lower limits of strain during that cycle.

### 2.2 Microscale Theoretical Model of Chloride-Ion Diffusion Coefficient

### 2.2.1 Determination of Chloride-Ion Diffusion Coefficient in Concrete Based on Multiphase Spherical Theory

According to reference (De and Mukherjee, 2020), the multiphase composite spherical model can effectively represent the microscale multiphase composite materials (Fig. 2a). The chloride-ion diffusion coefficient in concrete can be determined at the microscale using multiphase spherical theory. In this study, the multiphase composite spherical model is extended to a three-phase spherical model, as illustrated in Fig. 2b.



### (a) Multiphase composite spherical model



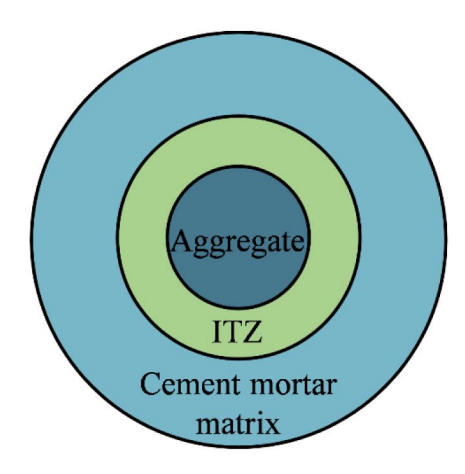
In this three-phase spherical model, the innermost sphere represents the coarse aggregate with a volume fraction of  $V_{\rm a}$  and a diffusion coefficient of  $D_{\rm a}$ . The interfacial transition zone (ITZ) is located in the second layer surrounding the coarse aggregate, with a volume fraction of  $V_{\rm I}$  and a diffusion coefficient of  $D_{\rm I}$ . The outermost layer is the cement mortar matrix, with a volume fraction of  $V_{\rm m}$  and a diffusion coefficient of  $D_{\rm m}$ . Generally, the permeability of the aggregate is significantly lower than that of the mortar and ITZ; therefore, it can be assumed that the chloride-ion diffusion coefficient of the coarse aggregate  $D_{\rm a}$  is 0. The chloride-ion diffusion coefficient  $D_{\rm c}$  of the three-phase spherical concrete model can be expressed as (Herve, 2002):

$$D_{\rm c} = D_{\rm m} \frac{2D_{\rm I} V_{\rm I} (2V_{\rm a} + 2V_{\rm I} + 1) + 2D_{\rm m} V_{\rm m} (3V_{\rm a} + 2V_{\rm I})}{D_{\rm m} (2 + V_{\rm a} + V_{\rm I}) (3V_{\rm a} + 2V_{\rm I}) + 2D_{\rm I} V_{\rm I} V_{\rm m}} \quad (18)$$

In Eq. (18),  $D_{\rm m}$  is the diffusion coefficient of the cement mortar (m²/s),  $D_{\rm I}$  is the diffusion coefficient of the interfacial transition zone (m²/s),  $V_{\rm a}$  is the volume fraction of the coarse aggregate (%),  $V_{\rm I}$  is the volume fraction of the interfacial transition zone (%), and  $V_{\rm m}$  is the volume fraction of the cement mortar (%).

### 2.2.2 Determination of Chloride-Ion Diffusion Coefficient in Cement Mortar and Interfacial Transition Zone

Based on the relationship between porosity, tortuosity, and shrinkage rate, the chloride-ion diffusion coefficient of cement mortar can be expressed as (Yu et al., 2019):



### (b) Three-phase spherical model of

### concrete

$$D_{\rm m} = \frac{D_0 \varphi_{\rm m} \delta_{\rm c}}{\tau} \tag{19}$$

In Eq. (19),  $D_{\rm m}$  represents the chloride-ion diffusion coefficient of the cement mortar (m²/s),  $\phi_{\rm m}$  is the damaged porosity of the cement mortar,  $\tau$  and  $\delta_{\rm c}$  are the tortuosity and constrictivity of the pore network, respectively, and  $D_0$  is the diffusion coefficient of chloride ions in water (m²/s).

The empirical relationship between the diffusion coefficient of chloride ions in water  $D_0$  and temperature T is given as (Yu et al., 2019):

$$D_0 = 0.03707 \times 10^{-9} (T - 273.15) + 0.70935 \times 10^{-9}$$
 (20)

Owing to the influence of tortuosity, the transport path of chloride ions in concrete pores is not linear but follows curved pore channels. In the diffusion equation, tortuosity is described how the complex microstructure of concrete affects the diffusion speed of chloride ions, causing a reduction in the transport speed along the diffusion direction. Nakarai et al. (2006) established the relationship between tortuosity and porosity, as expressed in the following equation:

$$\tau = -1.5 \tanh \left[ 8.0(\varphi_m - 0.25) \right] + 2.5 \tag{21}$$

However, the diffusion of chloride ions in concrete is not only influenced by pore tortuosity, but also by pore size distribution. Owing to the irregularity in the pore diameters within concrete, the diffusion rate of chloride ions decreases. This is because variations in pore diameters within the concrete cause slower diffusion. If the cross-sectional diameter of a pore is smaller than in other

regions, the overall diffusion rate of chloride ions within the pore network will decrease. The parameter for the reduction in diffusion rate caused by variations in pore diameters is referred to as the constrictivity  $\delta_{c}$ , as shown in Fig. 3.

The pore constrictivity can be expressed as (Ohno et al., 2021):

$$\delta_c = 0.395 \tanh \left\{ 8[(\log(r_{\rm cp}^{\rm peak}) + 6.2] \right\} + 0.405 \quad (22)$$

In Eq. (22),  $r_{\rm cp}^{\rm peak}$  represents the peak radius of the large capillary pores (nm).

The ITZ exists between the cement mortar and the aggregate, where the pore structure is more complex and contains a higher number of pores. Pan et al. (2015) derived the chloride-ion diffusion coefficient for the interfacial transition zone (ITZ) as follows:

$$D_{\rm I} = \left(\frac{139.434}{t_{\rm I}} + 1\right) D_{\rm m} \tag{23}$$

In Eq. (23),  $t_{\rm I}$  represents the thickness of the ITZ ( $\mu m$ ). At present the research on the thickness of the ITZ around coarse aggregates is not consistent. Studies by Yang and Su et al. (Hu, 2018) indicate that the ITZ thickness ranges from 30 to 50  $\mu m$ , and it was found that the difference in chloride-ion diffusion coefficient between 50  $\mu m$  and 80  $\mu m$  is negligible.

### 2.2.3 Determination of Volume Fractions of Cement Mortar and Interfacial Transition Zone

Based on the statistical geometry of composite materials, Garboczi et al. (1998) predicted the volume fraction of ITZ in concrete through the theory of surface nearest distance distribution function. The volume fraction of ITZ,  $V_{\rm I}$ , is expressed as:

$$V_{\rm I} = 1 - V_{\rm a} - (1 - V_{\rm a}) \exp\left[-\pi N_{\rm v} \left(n_1 t_{\rm I} + n_2 t_{\rm I}^2 + n_3 t_{\rm I}^3\right)\right]$$
(24)

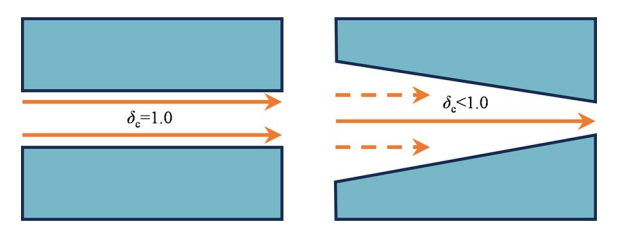


**Fig. 3** Schematic diagram of the reduction in chloride-ion diffusion rate caused by pore shape

$$N_{\rm V} = \begin{cases} \frac{6V_{\rm a} \left(d_{\rm amax}^{2.5} - d_{\rm amin}^{2.5}\right)}{5\pi \left(d_{\rm amin}^{2.5} d_{\rm amax}^{3} - d_{\rm amin}^{3} d_{\rm amax}^{2.5}\right)} (n = 2.5) \\ \frac{2V_{a} (d_{\rm amax}^{3} - d_{\rm amin}^{3})}{\pi d_{\rm amin}^{3} d_{\rm amax}^{3} \left(\ln d_{\rm amin} - \ln d_{\rm amin}\right)} (n = 3) \\ \frac{6(n - 3)V_{\rm a} \left(d_{\rm amax}^{n} - d_{\rm amin}^{n}\right)}{n\pi \left(d_{\rm amin}^{3} d_{\rm amax}^{n} - d_{\rm amin}^{n} d_{\rm amax}^{3}\right)} (\text{When } n \text{ is other values}) \end{cases}$$

$$(25)$$

$$\begin{cases} n_{1} = \frac{4\langle R^{2} \rangle}{1 - V_{a}} \\ n_{2} = \frac{4\langle R \rangle}{1 - V_{a}} + \frac{8\pi N_{v} \langle R^{2} \rangle^{2}}{(1 - V_{a})^{2}} \\ n_{3} = \frac{4}{3(1 - V_{a})} + \frac{16\pi N_{v} \langle R \rangle \langle R^{2} \rangle}{3(1 - V_{a})^{2}} + \frac{64A\pi^{2} N_{v}^{2} \langle R^{2} \rangle^{3}}{27(1 - V_{a})^{3}} \end{cases}$$
(26)

In the equation,  $N_{\rm v}$  represents the number of coarse aggregate particles per unit volume of concrete;  $d_{amin}$ and  $d_{\text{amax}}$  are the minimum and maximum diameters of the coarse aggregate particles (mm), respectively; n is the grading coefficient of the coarse aggregate; for equal volume fraction grading, n=3; for Fuller grading, n=2.5; R is the radius of the coarse aggregate particles (mm);  $\langle R \rangle, \langle R^2 \rangle, \langle R^3 \rangle$  are the average radius (mm), the square of the average radius (mm<sup>2</sup>), and the cube of the average radius (mm<sup>3</sup>) of the coarse aggregate particles, respectively; A is an approximation parameter that can take values of 0, 2, or 3. Garboczi et al.(1998) found that the parameter A has little effect on the results, and when A is set to 0, the calculated predictions align more closely with experimental results. The volume fraction of coarse aggregate  $(V_a)$  can be calculated from Table 3. The volume fractions of mortar, ITZ, and coarse aggregate are interrelated; therefore, the volume fraction of mortar  $(V_{\rm m})$  is equal to 1 minus the volume fractions of ITZ and coarse aggregate.

### 3 Experimental Materials and Methods

This study investigated chloride-ion migration tests on concrete under cyclic axial pressure. Combined with the equilibrium moisture content test, the porosity and pore distribution of the concrete were quantitatively characterized.

The main experimental process is illustrated in Fig. 4:

### 3.1 Materials

The cement is used with P.O 42.5 ordinary Portland cement, with an apparent density of  $3050~kg/m^3$ . Its chemical composition is shown in Table 1. The coarse aggregate is limestone gravel with a particle size of 5-16 mm, and the fine aggregate is medium sand with a fineness modulus of 2.69. The measured apparent densities



Fig. 4 Experimental flowchart

**Table 1** Chemical composition of cement

Main components	CaO	SiO <sub>2</sub>	Al <sub>2</sub> O <sub>3</sub>	MgO	SO <sub>3</sub>	Fe <sub>2</sub> O <sub>3</sub>
Content (%)	42.32	28.60	14.08	5.41	4.08	2.60

**Table 2** Gradation of coarse aggregate

Sieve aperture size (mm)	16	9.5	4.75	2.36	Sieve bottom
Passing percent	100	36.6	8.5	0.54	0

are 2700 kg/m $^3$  for the gravel and 2650 kg/m $^3$  for the sand. The gradation of the gravel, determined through sieve analysis, is shown in Table 2.

According to the provisions of JGJ 55-2011 "Standard for Mix Design of Ordinary Concrete" (Ministry of housing & urban-rural development of the People's Republic

Table 3 Concrete mix design ratio

Parameter	C-1	C-2	C-3
W/C	0.35	0.45	0.50
Water (kg/m³)	200	200	200
Cement (kg/m³)	571.0	444.0	400.0
Fine aggregate (kg/m³)	489.5	580.0	630.0
Coarse aggregate (kg/m³)	1089.0	1125.0	1120.0

of China, 2011), three different concrete specimens with varying water-to-cement ratios were designed according to the requirements for hydraulic concrete. The designed mix ratios for the experiments are shown in Table 3.

### 3.2 Cyclic Loading Test

The cyclic axial compression specimens were divided into 8 groups based on different cyclic loading conditions, with 3 cubic specimens of  $150 \times 150 \times 150$  mm in each group. For each water–cement ratio, 3 nondestructive concrete specimens were prepared as control groups simultaneously, as shown in Table 4. During the test, a cyclic axial compression load was applied to the specimens, compressing them to the target stress ratio. The cyclic axial compression stress ratio (stress level) is defined as the ratio of the applied stress to the compressive strength of the specimens. The specimens were first preloaded to the lower limit stress ratio (40%), followed by the first cyclic stage. Each cyclic stage consisted of 40 loading and unloading cycles until all cyclic stages of that condition were completed.

### 3.3 Equilibrium Moisture Content Test

After completing the cyclic loading, a core drill with an inner diameter of 100 mm was used to extract core samples from the concrete specimens. Subsequently, a cutting machine was employed to process the extracted samples into cylindrical specimens measuring  $100\times30$  mm for the equilibrium moisture content test.

The equilibrium moisture content test utilizes four salt solutions— $MgCl_2$ , NaBr, NaCl, and  $K_2SO_4$ —to create environments with different relative humidity (RH) levels. The actual relative humidity controlled by the saturated salt solutions is shown in Table 5.

Before conducting the equilibrium moisture content absorption test, the specimens are first immersed in water until saturated. During the immersion process, the specimens are weighed every 12 h (with surface water wiped off during weighing). When the mass change rate of the samples over a 24-h interval is less than 0.5%, the specimens are considered to have reached a saturated state. The specimens are then placed in an oven and dried at a temperature of  $60 \pm 2$  °C until completely dry. During the drying

**Table 5** The actual relative humidity controlled by the saturated salt solutions

Temperature (°C)	Saturated salt solution (%)					
	MgCl <sub>2</sub>	NaBr	NaCl	K <sub>2</sub> SO <sub>4</sub>		
20	32.73	55.87	77.78	94.66		

process, the specimens are weighed and recorded every 12 h (after cooling to room temperature), until the mass change rate between two consecutive weighings is less than 0.5%. At this point, the specimens are deemed to have reached a fully dry state, and the recorded mass is denoted as  $m_{\rm d}$ .

The specimens are then placed in a glass desiccator containing the prepared saturated salt solution, and the desiccators are sealed with plastic wrap. Subsequently, the glass desiccators are placed in a constant temperature and humidity chamber set at different temperatures. When the mass change of the specimens are less than 0.1% of the total mass during three consecutive weighings at intervals of at least 24 h, the specimens are considered to have reached equilibrium with the environment inside the desiccator, and the recorded mass at this point is denoted as  $m_{\rm w}$ . Finally, the moisture content of the specimens is characterized by the moisture content relative to the mass of the dried specimens, the process is shown in Fig. 5.

### 3.4 RCM Rapid Chloride Migration Test

The loaded specimens were cored and cut into cylindrical samples measuring 100×50 mm for the RCM test. A RCM-AIII type chloride-ion diffusion coefficient measurement instrument was used to conduct the rapid chloride migration test. Finally, the average value of the chloride-ion penetration depth was calculated based on the measured results, which was recorded as the color development depth, the process is shown in Fig. 6.

**Table 4** Table of cyclic axial compression test conditions for concrete

Specimen number	W/C	Cyclic load			Number of cycles	•
		Phase 1 (%)	Phase 2 (%)	Phase 3 (%)		strength (Mpa)
Y1	0.50	40~90	_	_	40	30
Y2		40~80	=	-	40	
Y3		40~70	=	-	40	
Y4		40~60	-	-	40	
Y5		40~80	40~80	-	80	
Y6		40~80	40~80	40~80	120	
Y7	0.45	40~80	_	-	40	32.6
Y8	0.35	40~80	_	_	40	39



Fig. 5 Equilibrium moisture content test



Fig. 6 RCM rapid chloride-ion migration test

The chloride-ion diffusion coefficient is calculated using the following formula:

$$\begin{cases} D_{\rm r} = 2.872 \times 10^{-6} \frac{Th(x - \alpha_{\rm f} \sqrt{x})}{t} \\ \alpha_{\rm f} = 3.338 \times 10^{-3} \sqrt{Th} \end{cases}$$
 (27)

In Eq. (27),  $D_{\rm r}$  represents the chloride-ion diffusion coefficient of concrete (m²/s), T is the temperature (K), h is the height of the specimen (m), x is the chloride-ion diffusion depth (m), t is the duration of the electrical test (s), and  $\alpha_{\rm f}$  is an auxiliary parameter.

### 4 Results and Discussion

### 4.1 Results of Cyclic Loading Test

The typical stress–strain curve of concrete under cyclic loading is shown in Fig. 5.

As shown in Fig. 7, the strain continuously increases with the ongoing cyclic loading. Although the same stress level is maintained for each cyclic load, the residual strain accumulates with the increase in the number of load cycles, leading to an increase in both the upper and lower strain limits of each cycle. At different upper

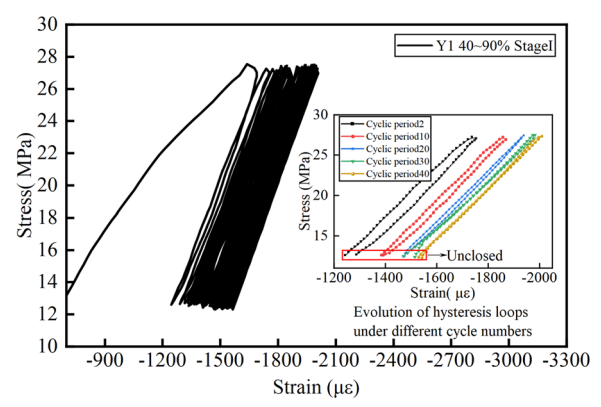


Fig. 7 Typical cyclic stress–strain curve of concrete

stress levels, the stress-strain curves exhibit a similar overall trend. In the early stages of cyclic loading, there is a significant gap between the stress-strain curves. As the loading cycles continue, the stress-strain curves gradually become denser, demonstrating a two-stage evolution pattern from sparse to dense as a whole.

By observing the stress–strain curves for a single cycle at different loading cycles in Fig. 7, it can be noted that an unclosed hysteresis loop is formed during the loading and unloading processes, taking on a narrow, leaf-like shape. This indicates that elastic deformation predominates during unloading, while plastic deformation is relatively small, resulting in a nonsmooth elliptical shape. This phenomenon is primarily attributed to the irreversible damage inflicted on the concrete's microstructure with each cyclic load, leading to the accumulation of residual strain (Chen et al., 2017).

Taking specimen Y1 as an example, during the initial loading phase, the increments of the upper and lower residual strains are relatively high. However, as the number of loading cycles increases, these values decrease rapidly, showing a distinct "negative exponential" characteristic, as illustrated in Fig. 8. Subsequently, the increments of residual strain enter a stable phase, fluctuating within a relatively small numerical range. The research in reference (Liu, 2020) shows that when the number of loading cycles reaches 90% of the fatigue life, the increments of residual strain in cement-based materials gradually increase with the number of cycles. Ultimately reach a maximum value before the specimen fails and exhibit a clear "U"-shaped evolution trend. In contrast, this study focuses on the damage caused by applying low-frequency cyclic loads. Because the failure stage has not been reached and the number of cyclic loads on the concrete specimen is relatively low. Therefore the overall increment of residual deformation for the specimen presents an "L"-shaped development trend.

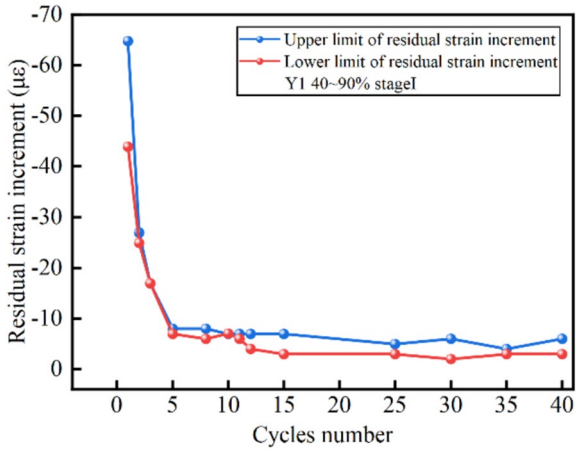


Fig. 8 Residual strain increment and cyclic number relationship

## 4.2 Results of Equilibrium Moisture Content Tests 4.2.1 Porosity of Concrete

et al., 2013).

Based on the equilibrium moisture content tests, the relationship between the equilibrium moisture content (w) of the specimens under different conditions and the relative humidity (h) is established. The experimental data is then fitted to an adsorption isotherm using Eq. (28) (Feng

$$w = \frac{Ckw_{\rm m}h}{(1 - kh)[1 + (C - 1)kh]}$$
 (28)

In Eq. (28), w: Equilibrium moisture content (%); h: Relative humidity (%);  $w_{\rm m}$ : Monolayer adsorption capacity (kg/m³); k: Multilayer adsorption energy parameter; C: Parameter related to the energy released during monolayer adsorption of moisture.

Taking the undamaged specimens with different water–cement ratios as an example, the adsorption isotherms of the undamaged specimens with different water–cement ratios are shown in Fig. 9.

According to literature (Zhang et al., 2023), the relationship between moisture content and pore size distribution is established using the density function method and pore size distribution function. By performing reverse calculations on the adsorption isotherms (Fig. 9), the initial porosity of the concrete specimens can be obtained, as shown in Fig. 10a. Similarly, the damaged porosity of the concrete after cyclic loading can also be determined, as illustrated in Fig. 10b.

Based on Fig. 10a, it can be seen that as the water-tocement ratio increases, the porosity of the concrete also increases. This is because there is evaporative moisture between some of the hydrated particles. As the water-to-cement ratio increases, the volume fraction of

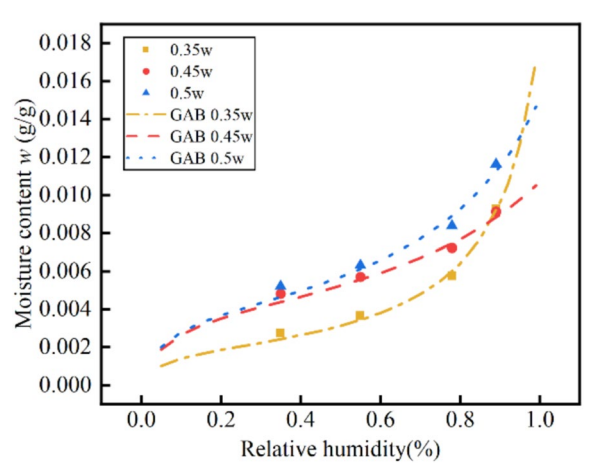


**Fig. 9** Adsorption isotherms of undamaged specimens with different water–cement ratios

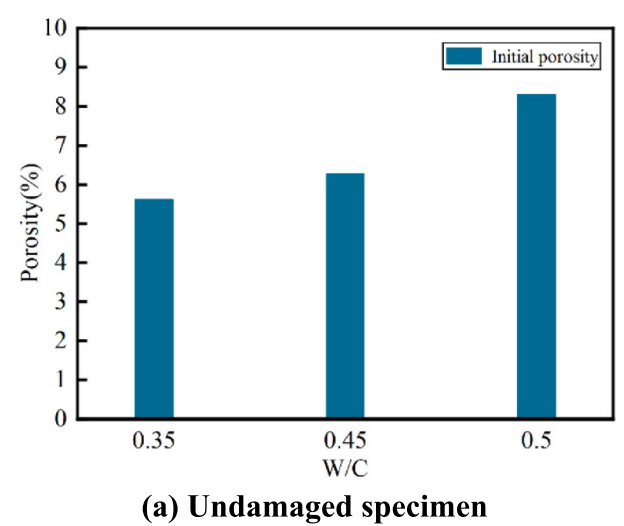
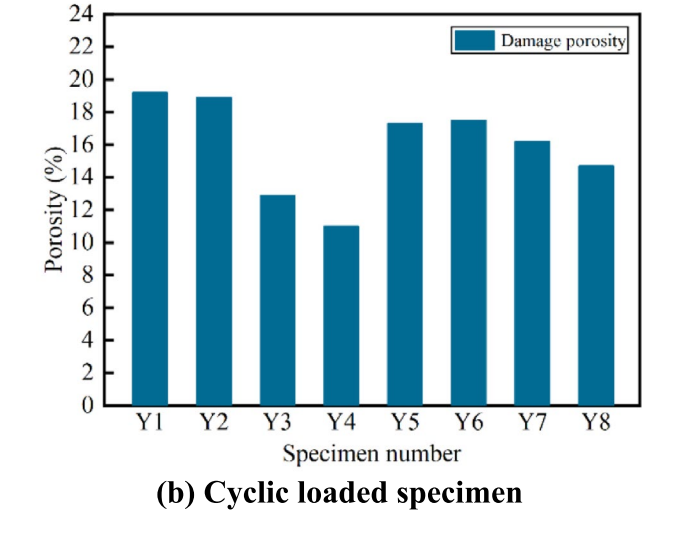


Fig. 10 Porosity of concrete before and after load application



moisture in the mortar correspondingly increases, resulting in more pores formed after evaporation. Observing Fig. 10b, it can be noted that as the stress level and number of cycles increase, the porosity of the concrete continually increases. This is because, under cyclic loading, damage within the concrete gradually accumulates, leading to changes in the microporous structure. Primary microcracks extend and connect, creating new secondary cracks at weak bonding areas in the matrix, thereby increasing porosity.

In each test group under different conditions, the porosity without load damage is at its minimum value. When the water-to-cement ratio is 0.5, the porosity of the undamaged specimen is 8.31%. As the upper limit of the stress level increases from 60 to 90%, the porosity of the compressed specimens increases by 32.4%, 55.2%, 127.4%, and 131% compared to the undamaged specimen, respectively. When the number of cycles increases from 40 to 120, the porosity increases by 127.4%, 108.2%, and 110.6%, respectively.

It can be concluded that when the water-to-cement ratio is 0.5, the porosity increases significantly with the increase in stress levels, showing no apparent limit. When the upper limit of the cyclic stress level is 80%, the increase in porosity grows by 2.3 times compared to the previous levels. This indicates that the damage to the concrete significantly increases when the upper limit of the cyclic stress level rises from 70 to 80%. The increase in porosity tends to become smaller as the number of loading cycles increases, but ultimately stabilizes.

#### 4.2.2 Pore Content of Concrete

Concrete contains pores of varying sizes, and under cyclic loading, its microstructural pore configuration may coarsen, potentially leading to the formation of new microcracks. This can result in changes in the content of pore groups within the concrete. The adsorption isotherm in this study's model is derived from the cumulative integral of the pore size distribution for different pore components at various relative humidity levels. The pore size distribution model accounts for the water contained in gel pores, small capillary pores, and large capillary pores. A typical pore size distribution curve for the compressed specimen Y3 is presented in Fig. 11.

As shown in Fig. 11, there is no distinct boundary between the sizes of gel pores and small capillary pores. The pore volumes of both pore groups overlap in a large

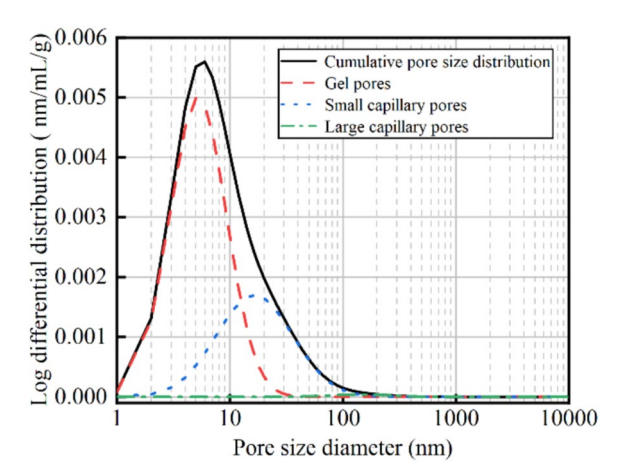


Fig. 11 Pore size distribution of different pore groups in specimen Y3

portion of the pore diameter range. The pore volumes of the two pore groups overlap in a large part of the pore diameter range. This observation is consistent with findings from certain microscopic experimental studies (Ranaivomanana et al., 2011). The size range of gel pores is approximately 1 nm to 12 nm, peaking around 5 nm. In comparison, small capillary pores have a relatively larger size range, from 5 to 100 nm, with a peak around 11 nm, while large capillary pores are predominantly found beyond 100 nm.

The proportion of the pore volume of each pore group relative to the total pore volume of the specimens is shown in Figs. 12 and 13. As illustrated in Fig. 12, after

the application of cyclic loading, the pore group content in concrete with different water-to-cement ratios exhibited a similar developmental trend. When compared with the undamaged specimens, the proportion of small capillary pores in the loaded specimens significantly decreased, while the proportion of large capillary pores increased noticeably. In contrast, the overall proportion of gel pores showed a slight increase.

As shown in Fig. 13a, under different upper stress levels, small capillary pores account for the highest proportion in all specimens. With the increase in stress level, the proportion of small capillary pores gradually rises, particularly in specimen Y1, where

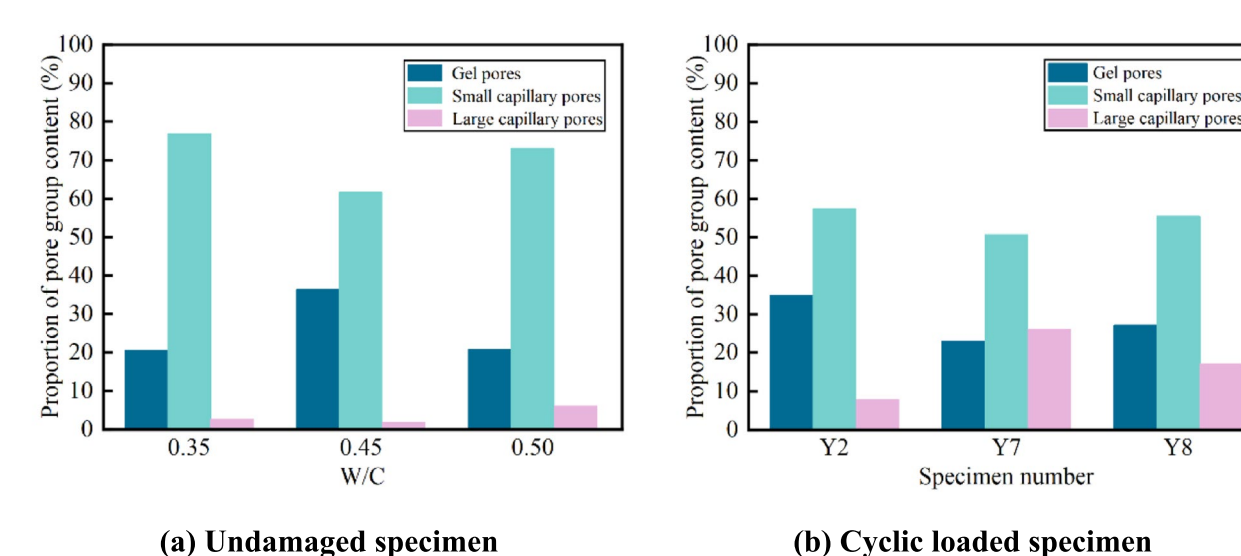


Fig. 12 Proportion of pore group content in concrete with different water-to-cement ratios

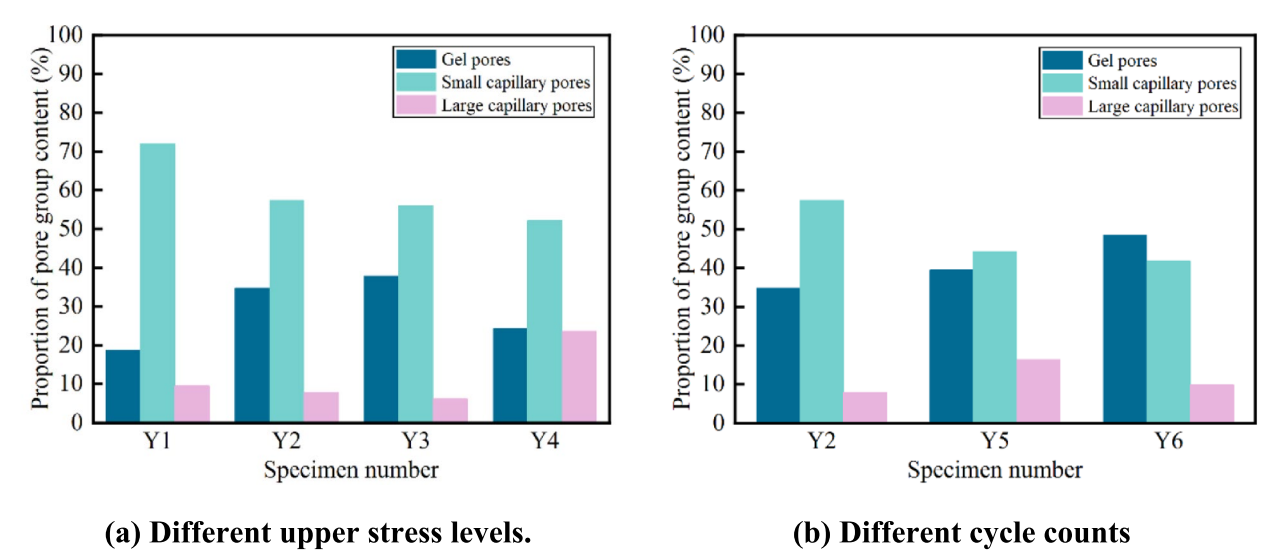


Fig. 13 Proportions of pore group content in specimens subjected to different loading conditions

it exceeds 70%. Concurrently, the proportion of gel pores decreases steadily, and when the upper stress level reaches 90%, the gel pores account for only 18.7%. Except for the lower stress level specimen Y4, the proportions of large capillary pores and gel pores exhibit opposing trends with increasing stress levels. This indicates that stress levels significantly affect the distribution of the pore structure within the concrete.

Further examining Fig. 13b, it can be observed that as the number of cycles increases, the proportions of gel pores and small capillary pores exhibit opposite trends, while the proportion of large capillary pores shows an overall increasing trend. This indicates that a higher number of cycles may facilitate the transformation of small capillary pores into large capillary pores or induce the formation of large capillary pores and gel pores. This leads to the coarsening of the pore structure within the concrete and an accompanying increase in porosity.

In summary, both stress level and the number of cycles significantly influence the pore structure within concrete. Under high stress levels, the proportion of small capillary pores increases. While a higher number of cycles exacerbates the coarsening of the pore structure, accompanied by an increase in large capillary pores and gel pores, thereby altering the porosity of the concrete.

### 5 Model Validation

In order to verify the rationality of the concrete chloride-ion diffusion coefficient model, Eq. (18) was used to calculate the chloride-ion diffusion coefficient, which was then compared with the measured values from the RCM test. In the calculation, the aggregate gradation was based on Fuller gradation, with n set to 2.5, the ITZ thickness ( $t_{\rm I}$ ) taken as 50  $\mu$ m, and the initial external distance ( $b_{\rm 0}$ ) for the two-phase spherical model set to 0.5. According to the pore size distribution curve of large capillary pores in Fig. 11, the pore size  $r_{\rm cp}^{\rm peak}$  of the specimen was taken as 550 nm. The mechanical properties of the mortar are shown in Table 6.

It is important to note that during the elastic deformation phase, when concrete is subjected to axial pressure, the pores will become denser due to compression. However, after undergoing cyclic loading at higher stress levels, the internal pore structure of the concrete may undergo varying degrees of change. Some pores potentially expanding while others may contract. This model

**Table 6** Mechanical properties of the pore-free mortar matrix

Material	Elastic modulus (GPa)	Bulk modulus (GPa)	Shear modulus (GPa)	Poisson's ratio
Pore-free mortar matrix	30.1	22.5	11.8	0.28

only considers the scenario where the porosity increases as a result of loading. The comparison results between the model predictions and the RCM test values are shown in Fig. 14.

As can be seen from Fig. 12, the minimum value of the model predicted values is 9.422, the maximum value is 37.628, the average value is 18.7965, and the standard deviation is approximately 9.8178. The minimum value of the test values is 4.966, the maximum value is 64.896, the average value is 22.7565, and the standard deviation is approximately 20.1981. The correlation coefficient  $R^2$ =0.65. The results indicate that this model can predict the evolution law of the chloride-ion diffusion coefficient of concrete under cyclic loading quite well. When the chloride-ion diffusion coefficient is less than 22×10<sup>-12</sup> m<sup>2</sup>/s, the model error is small and the applicability is good. However, when the chlorideion diffusion coefficient is greater than  $22 \times 10^{-12}$  m<sup>2</sup>/s, the error is large. This may be because under high stress levels or multiple cyclic loadings, the damage degree of the concrete is intensified, resulting in the expansion and connection of the original microcracks. At the same time, new secondary cracks are generated at the weak bonding areas of the matrix, which provides potential channels for the transmission of chloride ions; thus, increasing the chloride-ion diffusion coefficient of the concrete. In addition, more plastic deformation may also lead to an increase in the deviation of the model prediction.

### **6 Model Parameter Analysis**

### 6.1 Influence of Initial Porosity on the Chloride-Ion Diffusion Coefficient of Mortar

Volume strain is a key parameter affecting the damage porosity of mortar. Therefore, when studying the variation of the chloride-ion diffusion coefficient of cement mortar with initial porosity, the influence of volume

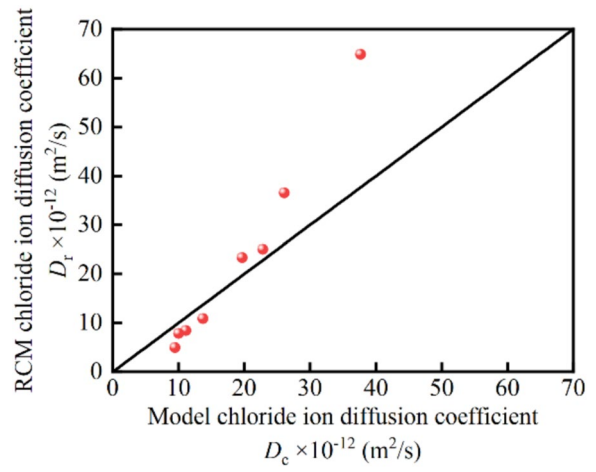


Fig. 14 Comparison of model predictions and RCM test values

strain is taken into account. In this parameter study, it is assumed that the mortar is subjected to cyclic axial compressive loading, with the value of  $r_{\rm cp}^{\rm peak}$  set at 550 nm and the volume fraction of coarse aggregate taken as 0.4. The volume strains are set at 1, 1.5, 2, and 2.5, while the initial porosity of the mortar ranges from 0.05 to 0.4. The influence of initial porosity on the chloride-ion diffusion coefficient of mortar is illustrated in Fig. 15.

As shown in Fig. 15, the chloride-ion diffusion coefficient of cement mortar increases with the initial porosity. When the initial porosity is less than 0.1, the growth trend of the chloride-ion diffusion coefficient is quite evident, but it remains below  $4 \times 10^{-11}$  m<sup>2</sup>/s. During the process of increasing the initial porosity from 0.1 to 0.3, the chloride ion diffusion coefficient rises sharply. In addition, when the initial porosity reaches 0.3, the chloride-ion diffusion coefficient exceeds  $10 \times 10^{-11}$  m<sup>2</sup>/s. This indicates that within the range of initial porosity from 0.1 to 0.3, the influence of cyclic loading on the chloride-ion diffusion coefficient is more significant. This is mainly because, when the initial porosity is relatively low, the damage to the concrete under cyclic loading may be greater, thereby enhancing its effect on the chloride-ion diffusion coefficient. Furthermore, under the same initial porosity conditions, as the volume strain increases, the chloride-ion diffusion coefficient of the mortar also increases accordingly.

### 6.2 Influence of Tortuosity and Shrinkage on the Chloride-Ion Diffusion Coefficient of Concrete

At the micro scale, the chloride-ion diffusion coefficient of concrete is influenced by two microstructural parameters: tortuosity and shrinkage ratio. In this parameter study, it is assumed that concrete is subjected to cyclic

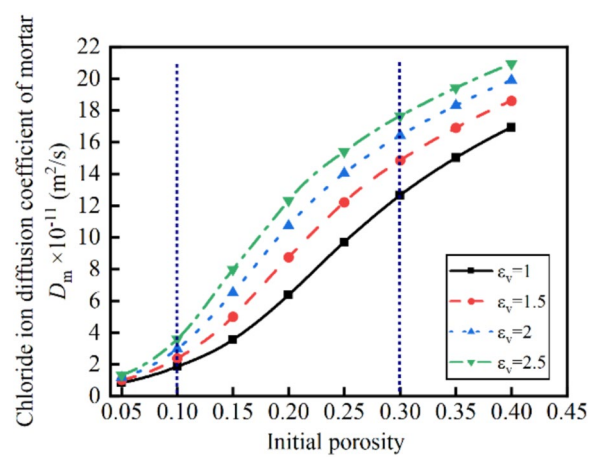


**Fig. 15** Relationship between chloride-ion diffusion coefficient of mortar, initial porosity, and volume strain

axial compressive loading. The coarse aggregate particle size ranging from 5 to 15 mm, a coarse aggregate volume fraction  $(V_{\rm a})$  of 0.4, and a volume strain of 1.55. The tortuosity values are set at 1.5, 2, 2.5, 3, and 3.5, while the shrinkage ratio varies from 0 to 0.4. The effects of the shrinkage ratio and tortuosity on the chloride-ion diffusion coefficient of concrete are illustrated in Fig. 16.

From Fig. 16, it can be observed that the chlorideion diffusion coefficient of concrete increases linearly with the increase in the shrinkage ratio. Under the same shrinkage ratio conditions, the chloride-ion diffusion coefficient gradually decreases as tortuosity increases. Furthermore, at any given shrinkage ratio, the growth rate of the chloride-ion diffusion coefficient remains consistent for the same tortuosity. When the shrinkage ratio is 0.01, the chloride-ion diffusion coefficient with a tortuosity of 1.5 is higher by  $1.354 \times 10^{-12}$  m<sup>2</sup>/s than that with a tortuosity of 3.5. However, when the shrinkage ratio increases to 0.4, the difference between the two expands to  $5.417 \times 10^{-11}$  m<sup>2</sup>/s. This indicates that the tortuosity effect and pore connectivity have a significant impact on the chloride-ion transport velocity. As the shrinkage ratio increases, concrete with lower tortuosity exhibits a significantly higher growth rate of the chloride-ion diffusion coefficient compared to that with higher tortuosity. This further suggests that the greater the tortuosity and the more complex the microstructure of the concrete, the lesser the influence of load damage on the chloride-ion diffusion coefficient.

### 6.3 Influence of Three-Phase Volume Fractions on the Chloride-Ion Diffusion Coefficient of Concrete

According to Eq. (18), the chloride-ion diffusion coefficient of concrete is influenced by the volumetric fractions

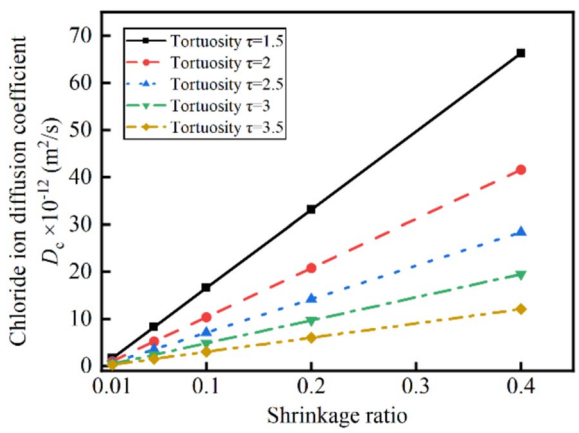


**Fig. 16** Effects of shrinkage ratio and tortuosity on the chloride-ion diffusion coefficient of concrete

of the three-phase materials. In order to eliminate the impact of the values of the chloride-ion diffusion coefficient  $D_{\rm m}$  for the mortar and  $D_{\rm I}$  for the interfacial transition zone (ITZ), Eq. (18) has been nondimensionalized, as shown in Eq. (29).

$$\frac{D_{\rm c}}{D_{\rm m}} = \frac{2D_{\rm I}/D_{\rm m}V_{\rm I}(2V_{\rm a}+2V_{\rm I}+1) + 2V_{\rm m}(3V_{\rm a}+2V_{\rm I})}{(2+V_{\rm a}+V_{\rm I})(3V_{\rm a}+2V_{\rm I}) + 2D_{\rm I}/D_{\rm m}V_{\rm I}V_{\rm m}} \tag{29}$$

Assuming that the concrete is subjected to cyclic axial compressive loads. The coarse aggregate particle sizes ranging from 5 to 15 mm, a volume strain of 1.55, and a damage porosity of the mortar set at 0.3.The volumetric fractions of coarse aggregate  $V_{\rm a}$  are taken as 0.3, 0.4, and 0.5, respectively. Based on Eqs. (24) to (26), the corresponding volumetric fractions of the interfacial transition zone (ITZ)  $V_{\rm I}$  are calculated to be 0.027, 0.036, and 0.045, while the volumetric fractions of the mortar  $V_{\rm m}$  are determined to be 0.67, 0.56, and 0.46, respectively.

Furthermore, the chloride-ion diffusion coefficient of concrete is influenced by the volumetric fraction, which also depends on the relative diffusivity of the ITZ and the mortar. Generally, the chloride-ion diffusion coefficient in the ITZ is between 1.3 and 16 times that of the mortar (Thilakarathna et al., 2020). In this parameter study, the ratio  $D_{\rm I}/D_{\rm m}$  is set at 3, 6, 9, 12, and 15. The evolution of the chloride-ion diffusion coefficient for different volumetric fractions of coarse aggregate and varying  $D_{\rm I}/D_{\rm m}$  ratios is illustrated in Fig. 17.

From Fig. 17, it can be observed that, under the same volumetric fraction of coarse aggregate, the ratio  $D_{\rm c}/D_{\rm m}$  increases with the rising  $D_{\rm I}/D_{\rm m}$ . That is, the chloride-ion diffusion coefficient  $D_{\rm c}$  of concrete improves as the diffusion coefficient  $D_{\rm I}$  in the interfacial transition zone (ITZ)

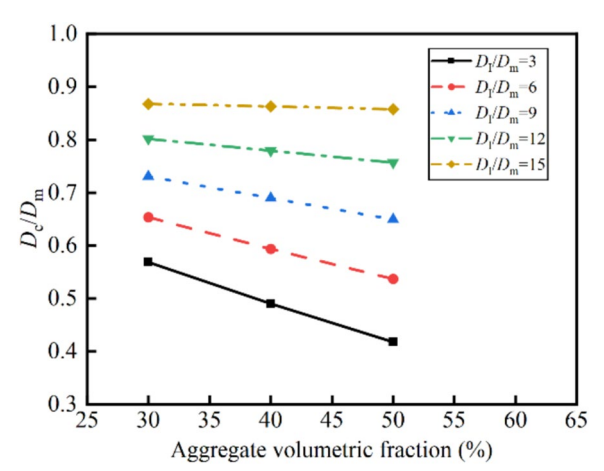


**Fig. 17** Evolution of chloride-ion diffusion coefficient of concrete under different volumetric fractions of coarse aggregate and varying  $D/D_m$  ratios

increases. When  $D_{\rm I}/D_{\rm m}=15$  the development of  $D_{\rm c}/D_{\rm m}$ becomes relatively stable with an approximate value of 0.86 as the volumetric fraction of coarse aggregate increases. This suggests that in scenarios where the diffusion coefficient in the ITZ is higher, the increased pore content in the ITZ provides more pathways for chlorideion transport, offsetting the blocking effect of the coarse aggregate on chloride-ion diffusion. Consequently, the overall influence of increased coarse aggregate volumetric fraction on the chloride-ion diffusion coefficient of concrete is not significant. Conversely, when  $D_{\rm I}/D_{\rm m}$  < 15,  $D_c/D_m$  remains below 0.86 and gradually decreases with the increase in coarse aggregate volumetric fraction, exhibiting a pronounced increase in slope. This indicates that when the diffusion coefficient in the ITZ is lower, the increase in the volumetric fraction of coarse aggregate outweighs the contribution of the ITZ, leading to a reduction in the chloride-ion diffusion coefficient of concrete.

### 7 Conclusions

In this study, the damage test of concrete under cyclic axial compression load was carried out. Based on this, the chloride-ion migration test and the equilibrium moisture content test were completed, and the porosity and pore group content of the concrete were quantitatively characterized. Furthermore, a theoretical model of the multiscale chloride-ion diffusion coefficient of concrete under cyclic load was established. According to the analysis of the test results and model predictions, the following conclusions are drawn:

- (1) Under cyclic loading, the stress-strain curves in the loading and unloading sections do not coincide, forming an unclosed hysteresis loop. Each cyclic loading causes irreversible residual strain in the concrete, driving the stress-strain curve to evolve in the direction of increasing strain.
- (2) The porosity of concrete increases with the increase of the water–cement ratio, stress level and the number of cycles. When the upper limit value of the stress level is increased to 80%, the damage increases geometrically. Cyclic loading promotes the transformation of small capillary pores into large capillary pores, resulting in the coarsening of the pore structure inside the concrete, and the porosity increases accordingly. For the specimen with a water–cement ratio of 0.5 under a stress level of 90%, the porosity increases by 131% compared with the undamaged state (from 8.31 to 19.23%). The analysis of microscopic pore group reconstruction shows that the proportion of large capillary pores (>100 nm) increases from the ini-

- tial 6.3–18.9%, while the proportion of small capillary pores (5-100 nm) decreases by 27.5%. When the number of cycles increases from 40 to 120, the increase rate of porosity shows a decreasing trend  $(127.4\% \rightarrow 108.2\% \rightarrow 110.6\%)$ , indicating that there is a threshold effect in the damage evolution.
- (3) When the chloride-ion diffusion coefficient is less than  $22 \times 10^{-12}$  m<sup>2</sup>/s, the model has a small error and good applicability. When it is greater than this value, the damage under cyclic loading is intensified, and more plastic deformation also leads to a slight increase in the predicted deviation of the model. The established mesoscopic diffusion model has good applicability in the range of  $D_c < 22 \times 10^{-12}$ m<sup>2</sup>/s, and the error increases when it exceeds this threshold (the maximum deviation reaches 34.6%). The parameter analysis shows that when D<sub>I</sub>/  $D_m = 15$ , increasing the volume fraction of coarse aggregate from 30 to 50% only reduces D<sub>c</sub>/D<sub>m</sub> by 8.7%; while when  $D_I/D_m=3$ , the same increment of aggregate can reduce  $D_{c}/D_{m}$  by 31.2%, confirming that the high permeability of the ITZ will significantly weaken the barrier effect of the aggregate.
- (4) When the initial porosity is in the range of 0.1-0.3, for every 0.5 unit increase in the volume strain, the chloride-ion diffusion coefficient increases by 63-127%. When the tortuosity increases from 1.5 to 3.5, the sensitivity of the shrinkage rate to D<sub>c</sub> decreases by 42%, indicating that the complex pore structure can buffer the enhanced transmission effect of load damage.

#### List of symbols

- Initial porosity (%)  $\varphi_0$
- Damaged porosity (%)  $\varphi_{m}$
- Initial inner radius (mm)  $a_0$
- $b_0$ Initial outer radius (mm)
- Inner radius after loading (mm)
- Outer radius after loading (mm)
- Radial enforced displacement ū
- Radial displacement component of sphere (mm)
- Radial body force (N)
- Distance from sphere center to boundary (mm)
- Poisson's ratio of solid matrix material
- Ε Elastic modulus of solid matrix material (GPa)
- Radial stress component  $\sigma_r$
- Axial stress component  $\sigma_{\theta}$
- Radial displacement field  $u_{\rm rm}$
- $\sigma_{\rm rm}$
- Bulk modulus of cement mortar phase (Gpa)
- Shear modulus of cement mortar phase (Gpa)  $\mu_{\rm m}$
- Radial displacement field of spherical pore  $U_{\rm rp}$
- Radial stress field
- Bulk modulus of pore medium (Gpa)
- Volumetric strain
- Ď<sub>s</sub> K\* Damage variable
- Bulk modulus
- Shear modulus
- Initial elastic modulus of cement mortar unit (Gpa)

- Poisson's ratio of cement mortar unit
- Axial length of specimen (mm)
- Strain under uniaxial loading, corresponding to residual strain in this
- Initial loading elastic modulus of concrete
  - Unloading elastic modulus at current cycle number
- Diffusion coefficient of cement mortar (m<sup>2</sup>/s)
- Diffusion coefficient of interfacial transition zone (ITZ) (m<sup>2</sup>/s)
- Volume fraction of coarse aggregate (%)
- Volume fraction of interfacial transition zone (%)
- Volume fraction of cement mortar (%)
- Diffusion coefficient of coarse aggregate (m<sup>2</sup>/s), taken as 0
- $D_{c}$ Chloride-ion diffusion coefficient of three-phase spherical concrete
- $D_0$ Chloride-ion diffusion rate in water (m<sup>2</sup>/s)
- Tortuosity of pore network
- Constriction factor of pore network
  - Peak radius of large capillary pores (nm)
- Thickness of ITZ (µm)
- Number of coarse aggregate particles per unit volume of concrete
- Coefficient of coarse aggregate gradation type
- Minimum diameter of coarse aggregate particles (mm) Maximum diameter of coarse aggregate particles (mm)
- Chloride-ion diffusion coefficient of concrete (m<sup>2</sup>/s)
- Temperature (K)
- h Height of specimen (m)
- Chloride-ion diffusion depth (m)
- Duration of electrical test (s)
- Auxiliary parameter

#### **Acknowledgements**

This work was supported by the National Natural Science Foundation of China (Grant No. 51509084); Open Foundation of National Engineering Research Center of High-speed Railway Construction Technology (Grant No. HSR202104); Open Project Program of Henan Key Laboratory of Grain and Oil Storage Facility & Safety, Henan University of Technology (Grant No. 2022KF01); Cultivation Project for National Natural Science Foundation of China of Henan University of Technology (Grant No. 2024PYJH008); Key Research and Development Project of Henan Province (Grant No. 241111322600).

#### **Author contributions**

All authors contributed to the study. Qingzhang zhang made a contribution to conception, design of the work and revised the manuscript. Mengzhe Zhao made a contribution to conduct the experimental test, analysis the test results and drafted the manuscript. Li Song made a contribution to revise the manuscript deeply. Yuhang Yang made a contribution to revise the manuscript. Jiaming He made a contribution to conduct the experimental test. All authors commented on previous versions of the manuscript. All authors read and approved the final manuscript.

This research was supported by the National Natural Science Foundation of China (Grant No. 51509084); Open Foundation of National Engineering Research Center of High-speed Railway Construction Technology (Grant No. HSR202104); Open Project Program of Henan Key Laboratory of Grain and Oil Storage Facility & Safety, Henan University of Technology (Grant No. 2022KF01); Cultivation Project for National Natural Science Foundation of China of Henan University of Technology (Grant No. 2024PYJH008); Key Research and Development Project of Henan Province (Grant No. 241111322600).

### Availability of data and materials

All data generated or analysed during this study are included in this published article.

### **Declarations**

#### Competing interests

No competing interests exists in the submission of this manuscript, and the manuscript is approved by all authors for publication. The author declare that the work described was original research that has not been published

previously, and not under consideration for publication elsewhere, in whole or in part.

Received: 12 February 2025 Accepted: 21 April 2025 Published online: 10 July 2025

#### References

- Chen, X., Bu, J., Fan, X., et al. (2017). Effect of loading frequency and stress level on low cycle fatigue behavior of plain concrete in direct tension. Construction and Building Materials, 133(15), 367–375. https://doi.org/10.1016/j.conbuildmat.2016.12.085
- De, S., & Mukherjee, A. (2020). A multiscale model including the effect of pores, aggregates and their interfaces for moisture diffusion in concrete. *Cement and Concrete Composites*, 111, 103595. https://doi.org/10.1016/j.cemconcomp.2020.103595
- Du, X., Jin, L., & Zhang, R. (2015). Chloride diffusivity in saturated cement paste subjected to external mechanical loadings. *Ocean Engineering*, *95*(1), 1–10. https://doi.org/10.1016/j.oceaneng.2014.11.028
- Feng, C., Janssen, H., Wu, C., et al. (2013). Validating various measures to accelerate the static gravimetric sorption isotherm determination. *Building and Environ*ment, 69(11), 64–71. https://doi.org/10.1016/j.buildenv.2013.08.005
- Fu, C., Ye, H., Jin, X., et al. (2016). Chloride penetration into concrete damaged by uniaxial tensile fatigue loading. *Construction and Building Materials*, 125, 714–723. https://doi.org/10.1016/j.conbuildmat.2016.08.096
- Garboczi, E., & Bentz, D. (1998). Multi-scale analytical/numerical theory of the diffusivity of concrete. Advanced Cement Based Materials, 8(2), 77–88. https://doi.org/10.1016/S1065-7355(98)00010-8
- Guan, B., Yng, T., Wu, J., et al. (2018). Chloride transport behavior of damaged concrete under alternating load. *Journal of Building Material*, 21(2), 304–308. https://doi.org/10.3969/j.issn.1007-9629.2018.02.021
- He, R., Fu, C., Ma, H., et al. (2020). Prediction of effective chloride diffusivity of cement paste and mortar from microstructural features. *Journal of Materials in Civil Engineering*, 32(8), 04020211. https://doi.org/10.1061/(ASCE)MT. 1943-5533.0003288
- Herve, E. (2002). Thermal and thermoelastic behaviour of multiply coated inclusion-reinforced composites. *International Journal of Solids and Structures*, *39*(4), 1041–1058. https://doi.org/10.1016/S0020-7683(01)00257-8
- Hu, S. W. (2018). Research on predictive model for concrete structure durability under multiple influencing factors. Changsha University of Science & Technology.
- Jin, J. F. (2012). Study on rock mechanical properties under coupled static–cyclic impact loadings. Central South University.
- Jin, H. S., Liu, J., Zhong, D. J., et al. (2023). Experimental study on chloride ion diffusion behavior and microstructure in concrete under alternating ambient humidity conditions. *Construction and Building Materials*, 401, 132886. https://doi.org/10.1016/j.conbuildmat.2023.132886
- Lee, B., Hyun, J., Kim, Y., et al. (2014). Chloride permeability of damaged highperformance fiber-reinforced cement composite by repeated compressive loads. *Materials*, 7(8), 5802–5815. https://doi.org/10.3390/ma7085802
- Li, Y., Shen, A., Lyu, Z., et al. (2020). Investigations of chloride ions permeability of pavement concrete under coupled effect of fatigue loading and hydrodynamic pressure. *International Journal of Pavement Engineering*, 23(5), 1659–1674. https://doi.org/10.1080/10298436.2020.1819540
- Liu, J. C. (2020). Study on the energy evolution law and damage characteristics of deformation and failure process of coral concrete. Nanjing University of Science & Technology.
- Liu, K., Cheng, X., Li, J., et al. (2019). Effects of microstructure and pore water on electrical conductivity of cement slurry during early hydration. *Composites*, 177, 107435. https://doi.org/10.1016/j.compositesb.2019.107435
- Liu, Q., Hu, Z., Wang, X., et al. (2022). Numerical study on cracking and its effect on chloride transport in concrete subjected to external load. *Construction and Building Materials*, 325, 126797. https://doi.org/10.1016/j.conbuildmat.2022. 126797
- Ministry of housing and urban-rural development of the People's Republic of China. (2011). *Code for design of concrete mix proportion (JGJ 55–2011)*. China Architecture & Building Press.
- Nakarai, K., Ishida, T., & Maekawa, K. (2006). Multi-scale physicochemical modeling of soil–cementitious material interaction. *Soils and Foundations*, 46(5), 653–663. https://doi.org/10.3208/sandf.46.653

- Ohno, M., Limtong, P., & Ishida, T. (2021). Multiscale modeling of steel corrosion in concrete based on micropore connectivity. *Journal of Building Engineering.*, 47, 103855. https://doi.org/10.1016/j.jobe.2021.103855
- Pan, Z., Chen, A., & Ruan, X. (2015). Spatial variability of chloride and its influence on thickness of concrete cover: a two-dimensional mesoscopic numerical research. *Engineering Structures*, 95, 154–169. https://doi.org/10.1016/j.engstruct.2015.03.061
- Ranaivomanana, H., Verdier, J., Sellier, A., et al. (2011). Toward a better comprehension and modeling of hysteresis cycles in the water sorption—desorption process for cement based materials. *Cement and Concrete Research*, 41(8), 817–827. https://doi.org/10.1016/j.cemconres.2011.03.012
- Rao, M., & Ramana, Y. (1992). A study of progressive failure of rock under cyclic loading by ultrasonic and AE monitoring techniques. *Rock Mechanics and Rock Engineering*, 25(4), 237–251. https://doi.org/10.1007/BF01041806
- Saito, T., Chijiwa, N., Shinozaki, H., et al. (2020). Mitigating bond deterioration under cyclic loading and water exposure. *Aci Structural Journal*, *117*(6), 51725885. https://doi.org/10.14359/51725885
- Thilakarathna, P., Baduge, K., Mendis, P., et al. (2020). Mesoscale modelling of concrete-a review of geometry generation, placing algorithms, constitutive relations and applications. *Engineering Fracture Mechanics*, 231, 106974. https://doi.org/10.1016/j.engfracmech.2020.106974
- Tong, L. Y., Liu, Q. F., Xiong, Q., et al. (2024). Modeling the chloride transport in concrete from microstructure generation to chloride diffusivity prediction. *Computer-Aided Civil and Infrastructure Engineering*. https://doi.org/10.1111/mice.13331
- Yang, C., Cho, S., & Wang, L. (2006). The relationship between pore structure and chloride diffusivity from ponding test in cement-based materials. *Materials Chemistry and Physics*, 100, 203–210. https://doi.org/10.1016/j. Matchemphys.2005.12.032
- Yu, Y., Chen, X., Gao, W., et al. (2019). Modelling non-isothermal chloride ingress in unsaturated cement-based materials. *Construction and Building Materials, 217*, 441–455. https://doi.org/10.1016/j.conbuildmat.2019.05.078
- Zhang, G., Yang, Z., Yan, Y., et al. (2021). Experimental and theoretical prediction model research on concrete elastic modulus influenced by aggregate gradation and porosity. *Sustainability*, *13*(4), 13041811. https://doi.org/10.3390/su13041811
- Zhang, Q., He, J., Song, L., et al. (2023). Theoretical model of water vapor absorption–desorption equilibrium of concrete considering the effect of temperature. *Construction and Building Materials*, 375, 130968. https://doi.org/10.1016/j.conbuildmat.2023.130968
- Zhang, Y., Wan, X., Hou, D., et al. (2018). The effect of mechanical load on transport property and pore structure of alkali-activated slag concrete. *Construction and Building Materials, 189*, 397–408. https://doi.org/10. 1016/j.conbuildmat.2018.09.009

### **Publisher's Note**

Springer Nature remains neutral with regard to jurisdictional claims in published maps and institutional affiliations.

**Qingzhang Zhang** Ph.D, Professor, Henan Key Laboratory of Grain and Oil Storage Facility & Safety, Henan University of Technology, Henan Zhengzhou 450001, China and College of Civil Engineering, Henan University of Technology, Henan Zhengzhou 450001, China.

**Mengzhe Zhao** Master Student, College of Civil Engineering, Henan University of Technology, Henan Zhengzhou 450001, China.

**Li Song** Ph.D, Professor, National Engineering Research Center of High-speed Railway Construction Technology, Hunan Changsha 410075, China.

**Yuhang Yang** Master Student, College of Civil Engineering, Henan University of Technology, Henan Zhengzhou 450001, China.

**Jiaming He** Master Student, College of Civil Engineering, Henan University of Technology, Henan Zhengzhou 450001, China.